Published in final edited form as:
J Mol Med (Berl). 2011 August ; 89(8): 753–769. doi:10.1007/s00109-011-0764-0.

Animal models and molecular imaging tools to investigate lymph node metastases

Elliot L. Servais,
Division of Thoracic Surgery, Memorial Sloan-Kettering Cancer Center, 1275 York Ave., New York, NY 10065, USA, Center for Cell Engineering, Memorial Sloan-Kettering Cancer Center, New York, NY, USA

Christos Colovos,
Division of Thoracic Surgery, Memorial Sloan-Kettering Cancer Center, 1275 York Ave., New York, NY 10065, USA, Center for Cell Engineering, Memorial Sloan-Kettering Cancer Center, New York, NY, USA

Adam J. Bograd,
Division of Thoracic Surgery, Memorial Sloan-Kettering Cancer Center, 1275 York Ave., New York, NY 10065, USA, Center for Cell Engineering, Memorial Sloan-Kettering Cancer Center, New York, NY, USA

Julie White,
Tri-Institutional Laboratory of Comparative Pathology, Memorial Sloan-Kettering Cancer Center, New York, NY, USA

Michel Sadelain, and
Center for Cell Engineering, Memorial Sloan-Kettering Cancer Center, New York, NY, USA, Department of Medicine, Memorial Sloan-Kettering Cancer Center, New York, NY, USA

Prasad S. Adusumilli
Division of Thoracic Surgery, Memorial Sloan-Kettering Cancer Center, 1275 York Ave., New York, NY 10065, USA, Center for Cell Engineering, Memorial Sloan-Kettering Cancer Center, New York, NY, USA

Prasad S. Adusumilli: adusumip@mskcc.org

Abstract

Lymph node metastasis is a strong predictor of poor outcome in cancer patients. Animal studies of lymph node metastasis are constrained by difficulties in the establishment of appropriate animal models, limitations in the noninvasive monitoring of lymph node metastasis progression, and challenges in the pathologic confirmation of lymph node metastases. In this comprehensive review, we summarize available preclinical animal cancer models for noninvasive imaging and identification of lymph node metastases of non-hematogenous cancers. Furthermore, we discuss the strengths and weaknesses of common noninvasive imaging modalities used to identify tumor-bearing lymph nodes and provide guidelines for their pathological confirmation.

Correspondence to: Prasad S. Adusumilli, adusumip@mskcc.org.

Elliot L. Servais and Christos Colovos contributed equally to this work.

Electronic supplementary material The online version of this article (doi:10.1007/s00109-011-0764-0) contains supplementary material, which is available to authorized users.

Disclosures The authors declare no competing financial interests.

Keywords

Mouse models; Metastasis; Immunology; Tumorigenesis; Malignancy; Imaging

Introduction

Lymphatic metastasis is a predictor of poor outcome in many solid malignancies [1–4]. The presence of lymph node metastases decreases the 5-year survival of melanoma patients independent of other prognostic factors of the primary tumor [5]. Likewise, the number of metastatic lymph nodes resected correlates with survival in breast cancer patients [6]. Despite the importance of lymph node metastasis (LNM), as highlighted by its inclusion in cancer staging systems, preclinical evaluation of lymph nodes (LN) in small animal models remains limited. When performing LNM studies, investigators face multiple challenges including: (1) the paucity of valid animal models in different animal species, (2) difficulties in identifying and serially monitoring metastatic disease by noninvasive imaging techniques, and (3) challenges of harvesting and pathologically confirming tumor replaced LN in small animal models. Herein, we review animal models, detail noninvasive imaging modalities, and provide recommendations for imaging, harvesting, and pathologically confirming LNM.

Preclinical LNM animal models

In this section, we review the most common, reproducible, murine models for LNM studies in non-hematogenous cancers (Table 1) and highlight the roles of: (1) immunocompetent versus immunodeficient hosts, (2) xenogeneic or syngeneic tumor models, and (3) orthotopic versus heterotopic tumor implantation. Employing syngeneic tumor cell lines or germline-encoded tumors in immunocompetent models of cancer provide a tumor microenvironment with compatible stromal, vascular, and immunological components [7]. Immunodeficient models utilize either human cancer cell lines or tumor explants as xenografts. These models lack a complete immunologic milieu for LNM but allow the use of well-characterized human cancer cell lines that may metastasize to regional nodal basins [8]. An understanding of the LN microenvironment and biology in commonly used immunodeficient mouse strains is essential for researchers investigating LNM as it is influenced by the immunologic milieu, therapy resistance, and the development of spontaneous cancers after a certain age (Supplemental Table 1). In addition to recognizing the benefits and limitations of the immune environment in animal models, it is essential to select a model that permits high-yield LNM for the specific cancer of interest. With an emphasis on reproducibility by multiple investigators, we summarize solid cancer animal models and cell lines useful for LNM studies (Tables 1 and 2) and highlight common murine LNM solid cancer models in the following sections.

Melanoma

A common model for studying lymphatic metastasis in melanoma involves orthotopic injection of syngeneic B16 melanoma cells into the footpad [9–12], auricular tissue [13, 14], thigh [15], or abdomen [16] of C57BL/6J mice (Table 1). LNM drain to local nodal basins resulting in popliteal and inguinal metastases from footpad tumors; cervical metastases from auricular tumors; and axillary, popliteal, or inguinal metastases from ventral and flank tumors in >90% of mice within 2–4 weeks. In this murine model, the primary tumor can be resected with minimal morbidity or mortality. Large, pigmented, superficial tumor-bearing nodes, which subsequently develop, facilitate noninvasive imaging and ex vivo analysis of involved nodes without requiring mouse sacrifice. Table 1 details all melanoma models available for LNM imaging studies. Immunodeficient murine models allow for the study of human and murine melanomas in an immunological naive background [17–19]. In addition

to providing a large animal model of LNM, spontaneous swine melanoma models are used to examine practical limitations of current imaging techniques [20–22].

Breast

Animal models for breast cancer lymphatic metastasis are based upon orthotopic implantation of tumor explants or cancer cells into mammary fat pads (Table 1). Such models allow for noninvasive LNM imaging of superficial LN after surgical resection of primary tumor. The most common murine models utilize immunodeficient mice injected with cells derived from human breast cancer patients, including those with a high propensity for LN metastasis (Table 2). Tumor cells are injected into the mammary fat pad and LNM are noted within 3–8 weeks in the axillary, brachial, cervical, inguinal, and popliteal basins depending on the proximity of the mammary fat pad inoculated with tumor [23–25]. Another method for establishing an orthotopic model with high tumor engraftment rates and consistent anatomic location involves the surgical implantation of a human breast cancer into the mammary fat pad of a female nude mouse [26, 27]. The resulting tumor is resected, trimmed free of necrotic tissue, homogenized, and surgically implanted into the mammary fat pad of another nude mouse. This technique results in axillary LN (55% of animals at day 106 post-implantation), lung (15%), and liver (10%) metastases [27].

Head and neck

To identify regional LNM associated with oropharyngeal squamous cell carcinoma, an orthotopic mouse model developed by Myers et al. [28] is used in LNM imaging studies. Xenogeneic tumor cells are injected into the anterior tongue of an immunodeficient host and regional metastases to cervical and mandibular nodes were noted within 2 weeks (Table 1). Superficial nodal basins identified by noninvasive imaging techniques are reproducible and easily accessible for surgical biopsy via a small cervical incision and permit histopathologic confirmation of metastatic LN [29].

Pleural/lung

In pleural cancer models, involved mediastinal nodal basins are difficult to image due to limitations in depth of penetration for many imaging modalities. Heterotopic preauricular models of mesothelioma metastasize to cervical LN and facilitate imaging of superficial nodal metastases while providing an easy method to study metastatic spread following primary tumor resection [30]. Our laboratory has developed an orthotopic xenograft model of human malignant pleural mesothelioma that accurately reflects human disease. Following the direct injection of cancer cells into the pleural space, bilateral pleural disease develops as the left and right pleural cavities communicate in mice. Nodal metastases to cervical, mediastinal, and retroperitoneal basins occur within 3 weeks of tumor inoculation. This model allows for noninvasive monitoring of tumor progression and quantitative bioluminescent imaging (BLI). BLI can identify tumor-bearing LN basins but does not permit the identification of specific LNM [31]. Tomographic methods, such as CT and MRI, are able to localize LNMs but are logistically challenging due to time constraints and the number of mice able to be screened.

In an orthotopic model of lung cancer described by Takizawa et al. [32], tumor cells suspended in Matrigel are directly injected into the lung parenchyma following a thoracotomy. Macroscopically detectable tumor typically develops at the injection site within 9 days with mediastinal LNM subsequently observed by 12 days [33]. Using this model, we have successfully developed protocols utilizing BLI to facilitate the identification and progression of mediastinal LNM. To histologically confirm mediastinal nodal involvement, LN must be harvested by carefully dissecting and mounting suspected nodal basins, even in the absence of macroscopic evidence of disease (as discussed in a later

section). To differentiate pleural tumor nodules from LNM, which grossly appear similar on harvesting, a detailed pathologic analysis by an experienced animal pathologist is the only useful confirmatory method.

Gastrointestinal/pancreatic

As with pleural and lung cancer models, gastrointestinal and pancreatic cancer can be challenging for LNM studies due to deep nodal basins. Commonly used models of these tumors are summarized in Table 1. A model of orthotopic gastric cancer described by Koyama et al. [34, 35] reproducibly develops LNM in nude rats following sub-serosal injection of the anterior stomach with a human scirrhous gastric carcinoma cell line with a predilection for lymphatic metastases (OCUM-2M LN). To further promote LNM, rats were depleted of natural killer cells with 3 Gy of irradiation 3 days prior to tumor inoculation [34, 35]. In animals with established tumor, fluorescent laparoscopy was used to identify lymphatic metastases, which were subsequently confirmed histologically. Orthotopic pancreatic cancer models [36, 37] utilize surgical implantation of human PaCa-2 cells into body of the pancreas of immunodeficient mice. On fluorescent imaging, mice exhibited significant primary tumor growth and metastatic spread within 2 weeks after surgical tumor implantation. In these studies, autopsy confirmed metastases in the spleen (100%), intestinal nodes (100%), portal nodes (90%), liver (80%), retroperitoneum (60%), diaphragm (50%), kidney (30%), and lungs (10%).

Prostate

LNM imaging studies for prostate cancer utilize heterotopic and orthotopic tumor implantation into host animals (Table 1). However, only orthotopic models recapitulate human disease with nodal metastases to pelvic and retroperitoneal LN [38, 39]. In this model, a highly metastatic human prostate cancer cell line (PC3-LN4) is injected into a lobe of the prostate and can result in 100% of mice with pelvic metastases as determined by BLI and fluorescent imaging.

Lymph node metastasis imaging in animal models

The successful development and use of LNM animal models are based on the ability to noninvasively, serially image and monitor LNM involvement. Even with a clear understanding of lymphatic anatomy, it is often difficult to grossly identify lymph nodes in small animal cancer models. Here, we review preclinical LN imaging modalities that direct the investigator to lymph nodes potentially harboring metastases by identifying nodal basins with an increased probability for metastases. We also describe techniques aimed at visualizing specific LNM.

Although radiocolloid and dye-based tracer agents are used in small animal models, their use for detecting LNM [40] can be limited by: (1) invasive surgical exploration or ex vivo analysis of specimens, (2) suboptimal spatial–temporal resolution in small animal models, and (3) high background signal from nearby tumors [41]. Newer modalities and tracer agents are being developed to overcome these limitations. Table 3 provides a summary of available LN imaging modalities used to identify both lymphatic architecture (Table 3a) and LNM (Table 4b).

Optimization of tracer agent size is fundamental for lymphatic mapping. Biokinetic and lymphoscintigraphy studies have shown that particle size impacts lymphatic entry and nodal retention of tracer molecules [42, 43]. An inverse relationship between particle size and LN interstitial clearance exists. Particles greater than 500 nm typically fail to reach tumor-draining lymph nodes (TDLN) due to slow interstitial clearance, while particles less than 5 nm can freely enter capillaries and pass directly through the LN. Intratumoral administration

of appropriately sized tracers (~5–150 nm) migrate into lymphatics, demonstrate retention within tumor draining LN [42, 44], and provide the basis for newer lymphatic tracer molecules, such as liposomes, dendrimers, and quantum dots.

Lymphatic nodal basins that can harbor LNM are best localized with imaging techniques that utilize exogenous tracer agents to define tumor-draining lymphatic beds (Table 3a). While specific LNM are best visualized with imaging techniques taking advantage of morphologic and functional changes in metastatic LN (Table 4b). In the following sections we describe tracer agents and imaging modalities for this purpose and detail characteristic properties including route of administration, imaging times, depth of penetration, and nodal specificity.

Liposomes—facilitate visual, radiographic, and ultrasonographic lymphatic imaging

Liposomes are lipid-based, vesicular, molecules that can be conjugated to or encapsulate various imaging agents, dyes, or radiocolloids. Ranging in diameter from 30 nm to several micrometers, the size and lipophilicity of liposomes promote efficient lymphatic entry and retention [45, 46]. Hirnle and colleagues [47–49] showed reliable SLN identification using blue dye-encapsulated liposomes administered subdermally in rabbit and pig models. Similarly, Phillips et al. [50] developed a blue dye/Tc-99m radio-colloid dual-labeled liposome, which allowed SLN identification more than a week following subdermal injection into rabbits. Dye-labeled liposomes migrate to lymphatic beds and are identified by direct visualization, surgical, or laparoscopic exploration. Radiocolloid-labeled liposomes require scintillation counters to localize tumor-draining lymphatic beds. To verify potential metastases, surgical intervention and tissue biopsy are needed. As an extension of dye-contrast ultrasonography, 5–10-μm microbubble-laden liposomes facilitate the identification of SLN by ultrasound. The tracer agent is injected subcutaneously, migrates through lymphatics, and identifies 85–95% of SLN—common sites of LNM [51, 52]. The disadvantages of US LN imaging include the limited use of identifying thoracic and retroperitoneal LN, operator experience, and ex vivo analysis of LN to confirm LNM. Although not currently utilizing liposomes/microbubbles, photoacoustic tomography (PAT) extends the ultrasonic depth of penetration by taking advantage of photoacoustic properties inherent to dye-contrast agents [53]. In mice and rats, PAT accurately detects LNs that accumulate low concentrations of methylene blue (~0.28 nM) at depths greater than 2 cm in both two- and three-dimensions [41, 54].

Quantum dots—fluorescent markers engineered for lymphatic migration and nodal retention

Quantum dots (QDs) are nearly spherical semiconductors with size-dependent fluorescence making these nanoparticles candidates for lymphatic imaging. QDs are engineered between 15 and 20 nm in diameter to optimize lymphatic migration and nodal retention [43]. QDs posses improved brightness, narrow emission spectra tunable across broad ranges, and enhanced photostability in comparison to organic fluorophores [19, 55, 56]. The physical properties of QDs are comprehensively reviewed by Biju et al. [57] and are beyond the scope of this review. In conjunction with a near infrared imaging (NIR) system, Parungo et al. [58, 59] showed that QDs demonstrate high yield localization of SLN in preclinical models of pleural and esophageal lymphatic drainage in rats. Similarly, Soltesz et al. [43] identified SLN following QD injection into lung parenchyma in 12/12 pigs within 5 min of injection at depths to 5 cm. QDs can accurately identify tumor-draining lymph nodes in animal models with no signs of acute systemic toxicities [19]. Potential problems of utilizing QD composed of heavy metals (e.g., cadmium, selenium) include cytotoxicity, tracer stability, and bioaccumulation which are catalogued by Hardman [60].

Optical frequency domain imaging with intravital microscopy—tracer-free lymphatic mapping

Although not validated for the identification of lymphatic metastases, emerging imaging techniques such as optical frequency domain imaging (OFDI) with intravital microscopy (IVM) offer high sensitivity and rapid acquisition times needed for large-volume lymphovascular morphometry [61]. Limited to superficial tumors modeled on dorsal skin folds, OFDI can perform high-resolution imaging of tumor vasculature, tracer-free functional lymphangiography, and characterization of tissue viability in the context of tumor burden and therapy. A priori knowledge of lymphatic anatomy is required to locate the lymph nodes and lymphatics draining from the dorsal skin fold model. OFDI allows for the identification of lymphovascular anatomy 1–2 mm from the surface, a more than two-fold increase from previous methods. Furthermore, the dynamic monitoring of lymphatic vasculature during cancer progression and lymphedema offers a potential method for evaluating existing and emerging therapies [61].

LNM-specific imaging techniques

The lymphatic tracer agents described above provide a means of lymphatic mapping but are not tumor cell specific. These techniques provide a roadmap to harvest cancer-draining lymph nodes for subsequent analysis for metastatic foci. Organic fluorophores conjugated to monoclonal antibodies targeting lymphatic-associated antigens have been utilized for the purposes of lymphatic mapping in combination with fluorescently labeled cancer cells to image metastatic LN. An anti-LYVE-1 monoclonal antibody (targeting the lymphatic endothelium) conjugated to AlexaFluor co-localized with fluorescently labeled meta-static pancreatic cancer cells migrating from inguinal to axillary LN through anterior abdominal wall lymphatics [62]. Similarly, Gleysteen et al. [63] identified cervical LNM in immunodeficient mice with oral squamous cell carcinoma using a tumor-targeted fluorescent anti-EGFR monoclonal antibody. This tumor-targeted strategy allows for specific imaging of tumor-involved LN. Furthermore, this method permits the study of LNM biology as demonstrated in a recent study showing that lymphangiogensis within TDLN is an early event in promoting LNM [64]. While targeted LN imaging using monoclonal antibodies has appeal, it can be hindered by non-specific uptake in visceral organs when administered intravenously [65] and by fluorophore properties. The long-term use of organic fluorophores is limited by poor tissue penetration, high levels of overlapping emission from background tissue autofluorescence and photobleaching [43, 45].

Oncolytic viruses—permit tumor-specific labeling with fluorescent proteins and identify LNM

Biological agents such as attenuated viruses [30, 66] and bacteria [67] selectively infect tumor cells, drain to TDLN, and help identify lymphatic tumor spread [30, 68, 69]. Oncolytic viruses selectively infect, replicate within, and lyse cancer cells. The virions released from lysed cancer cells infect neighboring cancer cells. When a single low dose of oncolytic virus is injected into a primary tumor, the virus traffics similar to tumor cells—from the primary tumor to the TDLN. When these draining nodes are superficial (axillary, femoral, or popliteal), LNMs can be identified by fluorescent microscopy. The replication-competent recombinant virus NV1066 (derived from HSV-1) carries a reporter gene for green fluorescent protein selectively infects cancer cells thereby facilitating the detection of nodal metastases with in vivo fluorescent imaging [30]. Our laboratory has shown the utility of identifying LNMs in the mediastinal region of pleural or lung cancer in an orthotopic mouse model utilizing fluorescent thoracoscopy. Furthermore, NV1066 was utilized to demonstrate the draining SLN in breast cancer metastases. In our experience, virally guided fluorescent imaging facilitates easy identification of metastatic LN from normal LN prior to histology and immunohistochemistry (Fig. 1). This modality offers decreased time and effort

needed to identify and harvest LNMs. Oncolytic virus-based LNM imaging with virally guided fluorescent reporters not only allows imaging and identification of LNM, but may also act as a therapeutic modality since the viruses selectively infect and lyse cancer cells. In addition to fluorescent imaging, this method offers a platform for in vivo LNM imaging and responses to therapy using viruses transduced to express BLI or positron emission tomography reporter genes [9, 26, 30, 66, 70–72].

Fluorescent-mediated molecular tomography—detects LNM and details immune interactions

Newer techniques are emerging which combine data from microscopic studies using intravital microscopy and mesoscopic imaging with fluorescent-mediated molecular tomography (FMT). These methods allow for serial, quantitative, and three-dimensional assessments of fluorophore concentrations in whole body imaging of murine cancer models [73]. Attenuation of signal from VT680-labeled (NIR-fluorescent probe) cells by surrounding tissue is decreased since hemoglobin, water, and lipids have their lowest absorption coefficients in the NIR region (650–900 nm). Although the tissue exhibits the lowest absorption coefficient in the NIR spectrum, there is still substantial absorption and scatter that limits depth of penetration. Using this technique, Swirski et al. tagged lymphocytes with VT680 and were adoptively transferred to a murine hind paw colon cancer model [74]. Mice are then serially imaged with FMT and IVM. FMT allows researchers to monitor T cells trafficking from a tumor focus to tumor-draining inguinal LN, at depths to 6 mm. Since VT680 does not lose fluorescence in resting cells, it is possible to quantify the number of adoptively transferred T cells within the ($\sim 7\times10^4$) tumor and the ($\sim 4\times10^4$) TDLN—consistent with ex vivo flow cytometric data ($\sim 4–10\times10^4$) [74]. Combined with IVM, this multi-modal method cannot only detect tumor-bearing LN, but also details the antigenic specificity of immunologic molecules in vivo.

Iron oxide nanoparticles—specifically detect LNM

Nanoparticles comprised of iron oxide can be used in MRI studies to accurately and sensitively detect LNM. The tracer agents ultra-small paramagnetic iron oxide or SPIO nanoparticles are administered intravenously and are selectively phagocytosed by macrophages. Based upon the T2*-weighted effects of iron oxide particles, normal functional lymphatic tissue with macrophages appears dark, while the nonphagocytic metastatic tissue appears bright. Although possible LNM in large, tumor-involved, LN, may be identified without tracer agents, studies by Lee et al. and Choi et al. combined gadolinium contrast agents with iron oxide nanoparticles to detect LNM larger than 0.5 cm with a sensitivity of 70–100% and specificity of 83–85% in rabbit models of head and neck cancer [75, 76].

Bioluminescent imaging

BLI sensitively assesses tumor progression and detects tumor metastases in live animal models [77, 78]. Tumor cells transduced to express luciferase emit light following the addition of substrate. The photon emissions from the cancer cells are detected by a cooled charge-coupled device camera, quantified, and represented as a photo overlay to identify tumor cell location. Our laboratory has applied BLI to detect LNM in mouse models of mesothelioma [31, 79] and lung [79] (Fig. 2) and prostate cancers [80]. Metastatic LN are best detected with mouse positioned ventrally (mediastinal nodes), laterally (cervical nodes), or dorsally (retroperitoneal/para-aortic nodes). Bioluminescent tumor models require optimization to maximize LNM identification and minimize technical limitations. Firefly luciferase is typically preferred in tumor models over wild-type click beetle luciferase due to a stronger bioluminescent signal [81]. Mutant click beetle luciferases engineered to emit specific wavelength photons overcome the limitation of enzyme heterogeneity and can

produce bright bioluminescent signals in vivo [82]. Marine luciferases, such as Gaussia and Reinella, are less favored due to rapid enzymatic kinetics and high background emissions. Transmission of bioluminescent signal depends upon the depth, viability, and vascularity of the tumor in addition to the scattering properties of blood and overlying tissue. Low tumor burden in metastatic LN decreases bioluminescent signal, possibly requiring longer exposure times (approximately three- to fourfold longer exposure, ~2 min), while large primary tumors may obscure signals from local LNM (as in the case of cervical LNM from models of head and neck cancers). Thus, parameters that may vary between animal models and require optimization include: substrate dose, route of substrate injection, time to imaging following substrate injection, image acquisition time, and mouse positioning. Furthermore, BLI has poor spatial resolution (1–2 mm) due to diffusely scattered photons and results in challenges to precisely localize tumor foci. Multi-modality imaging techniques, such as PET/CT data complemented by BLI, are being developed to address this limitation [83, 84]. As well, differential substrate specificities for beetle and marine luciferases (oxidizing D-luciferin or coelenterazine, respectively) allow for dual reporter systems. This system can be used for applications aimed at understanding biological mechanisms involved in metastases, (i.e., simultaneously tracking tumor and immune cells) [85]. Quantitative BLI of tumor burden is often limited by inherent properties due to the animal model used and extend to imaging LNM. Techniques aimed at the validation of quantitative BLI in various tumor models are described by several groups [31, 79, 86, 87]. Thus, BLI provides a sensitive and non-invasive technique for identifying and mapping LNM in addition to a platform for studying LNM biology.

Histopathological evaluation of LNM in mice

The imaging techniques described above provide accurate and efficient methods to noninvasively identify LNM in animal models. However, identification by bioimaging ultimately requires pathologic confirmation. The pathologic examination of murine LNM can be difficult, particularly in the setting of immunodeficient species and should involve an experienced comparative pathologist.

Gross evaluation of LN size and weight is not a reliable indicator of neoplastic involvement [88]. Systematic evaluation of specific TDLN basins can provide high yields of tumor-involved nodes. For a comprehensive overview of the anatomic details of the murine lymphatic system, we direct the reader to a study on mouse lymphatic anatomy by Van den Broeck et al. [89]. In this study, the authors catalog and illustrate the localization of murine LN after injection of India ink—providing a roadmap for LN harvesting required to confirm suspected metastases. Superficial LN (inguinal, axillary, or cervical/mandibular) are particularly easy to surgically resect and amenable to a variety of LN imaging modalities. However, identification and dissection of intracavitary nodes (intestinal, retroperitoneal, mediastinal, or pulmonary), often require fluorescent or tomographic imaging for identification. An “en bloc” dissection is often required to remove all the tissue in a nodal basin with subsequent LNM confirmation under high-power magnification using H&E staining and immunohistochemistry. Imaging techniques used to identify LNM in vivo can be extended to specifically identify the sites of metastases within an enlarged LN ex vivo [26] (Fig. 3).

Proper confirmation of tumor-involved LN requires evaluation of the size and cellularity of LN functional compartments, the presence of apoptosis, necrosis, and inflammation, hemorrhage, sinus histiocytosis and fat necrosis, and pigment accumulation [88, 90]. LN specimens exhibit considerable variation in histopathologic appearance due to differences in collection, embedding, and sectioning, as well as in individual differences depending on anatomic location and degree of inherent antigenic stimulation. The importance of

simultaneously evaluating control mice cannot be overstated. In comparison to the ease of identifying metastatic foci in preserved human and murine LN, investigators are often faced with the challenge of differentiating a LN totally or near totally replaced by tumor from a solitary tumor nodule (Fig. 4). In the setting of lymphatogenous metastases, total or near total replacement of LN by tumor can occur. Verification of LNM should include tumor immunohistochemistry as the gross appearance and architecture of LN may be distorted. Attention should be paid to the periphery of putative tumor-involved LN identifying islands of immune cells and preserved LN architecture with immunostaining. LNs from immunodeficient mouse strains have markedly different immunostaining patterns and architectures (Fig. 5).

Conclusions

The goal of LNM imaging studies is to identify and monitor the progression of metastases in animal models of cancer. Here, we provide an overview for selecting high-yielding LNM cell lines for representative common solid cancers and delineate their biokinetics and LNM yield in murine cancer models (Tables 1 and 2). Furthermore, we survey non-invasive imaging modalities appropriate for LNM cancer models, discuss their strengths and limitations, and describe the use of lymphatic specific and metastasis-specific tracer agents as well as emerging LNM imaging technologies. We provide recommendations to improve the sensitivity and specificity of identifying LNM and illustrate the potential of BLI to identify LNM based upon our laboratory's experience with murine models of mesothelioma, lung cancer, and prostate cancer. BLI provides a cost-effective means to screen large numbers of animals for LNM, and we highlight the use of tomographic methods in tandem with BLI to overcome its limitations in spatial–temporal resolution in order to precisely identify LNM. Finally, we detail the steps to ensure high yields of LNM identification and describe the precise spatial localization of characteristic immune cell lymph node architecture for a given species of mice—providing guidance in identifying LNM, even in lymph nodes completely replaced with tumor. In summary, this review provides a single platform for translational researchers to identify high-yielding LNM mouse models, non-invasive imaging modalities most commonly used to localize LNM, and the critical steps necessary to maximize yield and pathologic confirmation of LNM.

Supplementary Material

Refer to Web version on PubMed Central for supplementary material.

Acknowledgments

Funding This study was supported in part by American Association for Cancer Research (AACR) Translational Research Award, American Association for Thoracic Surgery (AATS)—Third Edward D. Churchill Research Scholarship, IASLC—International Association for the Study of Lung Cancer Young Investigator Award, National Lung Cancer Partnership/LUNGevity Foundation Research Grant, New York State Empire Clinical Research Investigator Program (ECRIP), Mesothelioma Applied Research Foundation (MARF), grant in memory of Lance S. Ruble and Stony Wold-Herbert Fund, and William H. Goodwin and Alice Goodwin and the Commonwealth Foundation for Cancer Research and the Experimental Therapeutics Center.

References

1. Giuliano AE, Kirgan DM, Guenther JM, Morton DL. Lymphatic mapping and sentinel lymphadenectomy for breast cancer. Ann Surg. 1994; 220:391–398. discussion 398–401. [PubMed: 8092905]
2. Govindarajan A, Baxter NN. Lymph node evaluation in early-stage colon cancer. Clin Colorectal Cancer. 2008; 7:240–246.10.3816/CCC.2008.n.031 [PubMed: 18650192]
3. Liptay M. Sentinel node mapping in lung cancer. Ann Surg Oncol. 2004; 11:271–274S.

4. Morton DL, Wen DR, Wong JH, Economou JS, Cagle LA, Storm FK, Foshag LJ, Cochran AJ. Technical details of intraoperative lymphatic mapping for early stage melanoma. Arch Surg. 1992; 127:392–399. [PubMed: 1558490]
5. Balch CM, Buzaid AC, Soong SJ, Atkins MB, Cascinelli N, Coit DG, Fleming ID, Gershenwald JE, Houghton A Jr, Kirkwood JM, McMasters KM, Mihm MF, Morton DL, Reintgen DS, Ross MI, Sober A, Thompson JA, Thompson JF. Final version of the American Joint Committee on Cancer staging system for cutaneous melanoma. J Clin Oncol. 2001; 19:3635–3648. [PubMed: 11504745]
6. Krag DN, Single RM. Breast cancer survival according to number of nodes removed. Ann Surg Oncol. 2003; 10:1152–1159. [PubMed: 14654470]
7. Teicher BA. Tumor models for efficacy determination. Mol Cancer Ther. 2006; 5:2435–2443.10.1158/1535-7163.MCT-06-0391 [PubMed: 17041086]
8. Kerbel RS. Human tumor xenografts as predictive preclinical models for anticancer drug activity in humans: better than commonly perceived-but they can be improved. Cancer Biol Ther. 2003; 2:S134–S139. [PubMed: 14508091]
9. Brader P, Kelly K, Gang S, Shah JP, Wong RJ, Hricak H, Blasberg RG, Fong Y, Gil Z. Imaging of lymph node micrometastases using an oncolytic herpes virus and [F]FEAU PET. PLoS ONE. 2009; 4:e4789.10.1371/journal.pone.0004789 [PubMed: 19274083]
10. Harrell MI, Iritani BM, Ruddell A. Tumor-induced sentinel lymph node lymphangiogenesis and increased lymph flow precede melanoma metastasis. Am J Pathol. 2007; 170:774–786.10.2353/ajpath.2007.060761 [PubMed: 17255343]
11. Kelly KJ, Brader P, Woo Y, Li S, Chen N, Yu YA, Szalay AA, Fong Y. Real-time intraoperative detection of melanoma lymph node metastases using recombinant vaccinia virus GLV-1h68 in an immunocompetent animal model. Int J Cancer. 2009; 124:911–918.10.1002/ijc.24037 [PubMed: 19035444]
12. Ruddell A, Harrell MI, Minoshima S, Maravilla KR, Iritani BM, White SW, Partridge SC. Dynamic contrast-enhanced magnetic resonance imaging of tumor-induced lymph flow. Neoplasia. 2008; 10:706–713. [PubMed: 18592009]
13. Hoshida T, Isaka N, Hagendoorn J, di Tomaso E, Chen YL, Pytowski B, Fukumura D, Padera TP, Jain RK. Imaging steps of lymphatic metastasis reveals that vascular endothelial growth factor-C increases metastasis by increasing delivery of cancer cells to lymph nodes: therapeutic implications. Cancer Res. 2006; 66:8065–8075.10.1158/0008-5472.CAN-06-1392 [PubMed: 16912183]
14. Rebhun RB, Lazar AJ, Fidler IJ, Gershenwald JE. Impact of sentinel lymphadenectomy on survival in a murine model of melanoma. Clin Exp Metastasis. 2008; 25:191–199.10.1007/s10585-008-9141-y [PubMed: 18264782]
15. Moore A, Sergeyev N, Bredow S, Weissleder R. A model system to quantitate tumor burden in locoregional lymph nodes during cancer spread. Invasion Metastasis. 1998; 18:192–197. [PubMed: 10640905]
16. Wunderbaldinger P, Josephson L, Bremer C, Moore A, Weissleder R. Detection of lymph node metastases by contrast-enhanced MRI in an experimental model. Magn Reson Med. 2002; 47:292–297.10.1002/mrm.10068 [PubMed: 11810672]
17. Galanzha EI, Shashkov EV, Tuchin VV, Zharov VP. In vivo multispectral, multiparameter, photoacoustic lymph flow cytometry with natural cell focusing, label-free detection and multicolor nanoparticle probes. Cytom A. 2008; 73:884–894.10.1002/cyto.a.20587
18. Kobayashi H, Ogawa M, Kosaka N, Choyke PL, Urano Y. Multicolor imaging of lymphatic function with two nanomaterials: quantum dot-labeled cancer cells and dendrimer-based optical agents. Nanomedicine Lond. 2009; 4:411–419.10.2217/nnm.09.15 [PubMed: 19505244]
19. Ballou B, Ernst LA, Andreko S, Harper T, Fitzpatrick JA, Waggoner AS, Bruchez MP. Sentinel lymph node imaging using quantum dots in mouse tumor models. Bioconjug Chem. 2007; 18:389–396.10.1021/bc060261j [PubMed: 17263568]
20. Boisgard R, Vincent-Naulleau S, Leplat JJ, Bouet S, Le Chalony C, Tricaud Y, Horak V, Geffrotin C, Frelat G, Tavitian B. A new animal model for the imaging of melanoma: correlation of FDG PET with clinical outcome, macroscopic aspect and histological classification in melanoblastoma-

bearing Libechov Minipigs. Eur J Nucl Med Mol Imaging. 2003; 30:826–834.10.1007/s00259-003-1152-y [PubMed: 12682788]

21. Goldberg BB, Merton DA, Liu JB, Thakur M, Murphy GF, Needleman L, Tornes A, Forsberg F. Sentinel lymph nodes in a swine model with melanoma: contrast-enhanced lymphatic US. Radiology. 2004; 230:727–734.10.1148/radiol.2303021440 [PubMed: 14990839]
22. Tanaka E, Choi HS, Fujii H, Bawendi MG, Frangioni JV. Image-guided oncologic surgery using invisible light: completed pre-clinical development for sentinel lymph node mapping. Ann Surg Oncol. 2006; 13:1671–1681.10.1245/s10434-006-9194-6 [PubMed: 17009138]
23. Dadiani M, Kalchenko V, Yosepovich A, Margalit R, Hassid Y, Degani H, Seger D. Real-time imaging of lymphogenic metastasis in orthotopic human breast cancer. Cancer Res. 2006; 66:8037–8041.10.1158/0008-5472.CAN-06-0728 [PubMed: 16912179]
24. Kobayashi H, Kawamoto S, Bernardo M, Brechbiel MW, Knopp MV, Choyke PL. Delivery of gadolinium-labeled nanoparticles to the sentinel lymph node: comparison of the sentinel node visualization and estimations of intra-nodal gadolinium concentration by the magnetic resonance imaging. J Control Release. 2006; 111:343–351.10.1016/j.jconrel.2005.12.019 [PubMed: 16490277]
25. Kobayashi H, Kawamoto S, Sakai Y, Choyke PL, Star RA, Brechbiel MW, Sato N, Tagaya Y, Morris JC, Waldmann TA. Lymphatic drainage imaging of breast cancer in mice by micro-magnetic resonance lymphangiography using a nano-size paramagnetic contrast agent. J Natl Cancer Inst. 2004; 96:703–708. [PubMed: 15126607]
26. Eisenberg DP, Adusumilli PS, Hendershott KJ, Chung S, Yu Z, Chan MK, Hezel M, Wong RJ, Fong Y. Real-time intraoperative detection of breast cancer axillary lymph node metastases using a green fluorescent protein-expressing herpes virus. Ann Surg. 2006; 243:824–830. discussion 830–822. 10.1097/01.sla.0000219738.56896.c0 [PubMed: 16772786]
27. Li X, Wang J, An Z, Yang M, Baranov E, Jiang P, Sun F, Moossa AR, Hoffman RM. Optically imageable metastatic model of human breast cancer. Clin Exp Metastasis. 2002; 19:347–350. [PubMed: 12090475]
28. Myers JN, Holsinger FC, Jasser SA, Bekele BN, Fidler IJ. An orthotopic nude mouse model of oral tongue squamous cell carcinoma. Clin Cancer Res. 2002; 8:293–298. [PubMed: 11801572]
29. Melancon MP, Wang Y, Wen X, Bankson JA, Stephens LC, Jasser S, Gelovani JG, Myers JN, Li C. Development of a macromolecular dual-modality MR-optical imaging for sentinel lymph node mapping. Invest Radiol. 2007; 42:569–578.10.1097/RLI.0b013e31804f5a79 [PubMed: 17620940]
30. Adusumilli PS, Eisenberg DP, Stiles BM, Chung S, Chan MK, Rusch VW, Fong Y. Intraoperative localization of lymph node metastases with a replication-competent herpes simplex virus. J Thorac Cardiovasc Surg. 2006; 132:1179–1188.10.1016/j. jtcvs.2006.07.005 [PubMed: 17059941]
31. Servais EL, Velez MC, Rusch VW, Sadelain M, Adusumilli PS. A preclinical mouse model of orthotopic pleural cancer that facilitates noninvasive quantitative monitoring of tumor progression and therapy response. Cancer Res. 2009; 69:B27.
32. Takizawa H, Kondo K, Toba H, Kenzaki K, Sakiyama S, Tangoku A. Fluorescence diagnosis of lymph node metastasis of lung cancer in a mouse model. Oncol Rep. 2009; 22:17–21. [PubMed: 19513499]
33. Ishikura H, Kondo K, Miyoshi T, Kinoshita H, Hirose T, Monden Y. Artificial lymphogenous metastatic model using orthotopic implantation of human lung cancer. Ann Thorac Surg. 2000; 69:1691–1695. [PubMed: 10892908]
34. Koyama T, Tsubota A, Nariai K, Mitsunaga M, Yanaga K, Takahashi H. Novel biomedical imaging approach for detection of sentinel nodes in an experimental model of gastric cancer. Br J Surg. 2007; 94:996–1001.10.1002/bjs.5650 [PubMed: 17380563]
35. Koyama T, Tsubota A, Nariai K, Yoshikawa T, Mitsunaga M, Sumi M, Nimura H, Yanaga K, Yumoto Y, Mabashi Y, Takahashi H. Detection of sentinel nodes by a novel red-fluorescent dye, ATX-S10Na (II), in an orthotopic xenograft rat model of human gastric carcinoma. Lasers Surg Med. 2007; 39:76–82.10.1002/lsm.20410 [PubMed: 17096413]
36. Bouvet M, Wang J, Nardin SR, Nassirpour R, Yang M, Baranov E, Jiang P, Moossa AR, Hoffman RM. Real-time optical imaging of primary tumor growth and multiple metastatic events in a pancreatic cancer orthotopic model. Cancer Res. 2002; 62:1534–1540. [PubMed: 11888932]

37. Katz MH, Bouvet M, Takimoto S, Spivack D, Moossa AR, Hoffman RM. Selective antimetastatic activity of cytosine analog CS-682 in a red fluorescent protein orthotopic model of pancreatic cancer. Cancer Res. 2003; 63:5521–5525. [PubMed: 14500389]
38. Kovar JL, Johnson MA, Volcheck WM, Chen J, Simpson MA. Hyaluronidase expression induces prostate tumor metastasis in an orthotopic mouse model. Am J Pathol. 2006; 169:1415–1426. [PubMed: 17003496]
39. Narla G, DiFeo A, Fernandez Y, Dhanasekaran S, Huang F, Sangodkar J, Hod E, Leake D, Friedman SL, Hall SJ, Chinnaiyan AM, Gerald WL, Rubin MA, Martignetti JA. KLF6-SV1 overexpression accelerates human and mouse prostate cancer progression and metastasis. J Clin Invest. 2008; 118:2711–2721.10.1172/JCI34780 [PubMed: 18596922]
40. Nwogu CE, Kanter PM, Anderson TM. Pulmonary lymphatic mapping in dogs: use of technetium sulfur colloid and isosulfan blue for pulmonary sentinel lymph node mapping in dogs. Cancer Investig. 2002; 20:944–947. [PubMed: 12449726]
41. Song L, Kim C, Maslov K, Shung KK, Wang LV. High-speed dynamic 3D photoacoustic imaging of sentinel lymph node in a murine model using an ultrasound array. Med Phys. 2009; 36:3724–3729. [PubMed: 19746805]
42. Bergqvist L, Strand SE, Persson BR. Particle sizing and biokinetics of interstitial lymphoscintigraphic agents. Semin Nucl Med. 1983; 13:9–19. [PubMed: 6220471]
43. Soltesz EG, Kim S, Laurence RG, DeGrand AM, Parungo CP, Dor DM, Cohn LH, Bawendi MG, Frangioni JV, Mihaljevic T. Intraoperative sentinel lymph node mapping of the lung using near-infrared fluorescent quantum dots. Ann Thorac Surg. 2005; 79:269–277. discussion 269–277. 10.1016/j.athoracsur.2004.06.055 [PubMed: 15620956]
44. Alazraki NP, Eshima D, Eshima LA, Herda SC, Murray DR, Vansant JP, Taylor AT. Lymphoscintigraphy, the sentinel node concept, and the intraoperative gamma probe in melanoma, breast cancer, and other potential cancers. Semin Nucl Med. 1997; 27:55–67. [PubMed: 9122724]
45. Jain R, Dandekar P, Patravale V. Diagnostic nanocarriers for sentinel lymph node imaging. J Control Release. 2009; 138:90–102.10.1016/j.jconrel.2009.05.010 [PubMed: 19445982]
46. Bar J, Herbst R, Onn A. Targeted drug delivery strategies to treat lung metastasis. Expert Opin Drug Deliv. 2009; 6:1003–1016. [PubMed: 19663628]
47. Dieter M, Schubert R, Hirnle P. Blue liposomes for identification of the sentinel lymph nodes in pigs. Lymphology. 2003; 36:39–47. [PubMed: 12755466]
48. Hirnle P, Harzmann R, Wright JK. Patent blue V encapsulation in liposomes: potential applicability to endolympatic therapy and preoperative chromolymphography. Lymphology. 1988; 21:187–189. [PubMed: 3199875]
49. Pump B, Hirnle P. Preoperative lymph-node staining with liposomes containing patent blue violet. A clinical case report. J Pharm Pharmacol. 1996; 48:699–701. [PubMed: 8866332]
50. Phillips WT, Klipper R, Goins B. Use of (99m)Tc-labeled liposomes encapsulating blue dye for identification of the sentinel lymph node. J Nucl Med. 2001; 42:446–451. [PubMed: 11337521]
51. Wang Y, Cheng Z, Li J, Tang J. Gray-scale contrast-enhanced utrasonography in detecting sentinel lymph nodes: an animal study. Eur J Radiol. 200910.1016/j.ejrad.2009.03.063
52. Wisner ER, Ferrara KW, Short RE, Ottoboni TB, Gabe JD, Patel D. Sentinel node detection using contrast-enhanced power doppler ultrasound lymphography. Invest Radiol. 2003; 38:358–365. [PubMed: 12908703]
53. Wang LV. Prospects of photoacoustic tomography. Med Phys. 2008; 35:5758–5767. [PubMed: 19175133]
54. Song KH, Stein EW, Margenthaler JA, Wang LV. Noninvasive photoacoustic identification of sentinel lymph nodes containing methylene blue in vivo in a rat model. J Biomed Opt. 2008; 13:054033.10.1117/1.2976427 [PubMed: 19021413]
55. Kim S, Lim YT, Soltesz EG, De Grand AM, Lee J, Nakayama A, Parker JA, Mihaljevic T, Laurence RG, Dor DM, Cohn LH, Bawendi MG, Frangioni JV. Near-infrared fluorescent type II quantum dots for sentinel lymph node mapping. Nat Biotechnol. 2004; 22:93–97.10.1038/nbt920nbt920 [PubMed: 14661026]

56. Dahan M, Laurence T, Pinaud F, Chemla DS, Alivisatos AP, Sauer M, Weiss S. Time-gated biological imaging by use of colloidal quantum dots. Opt Lett. 2001; 26:825–827. [PubMed: 18040463]
57. Biju V, Itoh T, Anas A, Sujith A, Ishikawa M. Semiconductor quantum dots and metal nanoparticles: syntheses, optical properties, and biological applications. Anal Bioanal Chem. 2008; 391:2469–2495.10.1007/s00216-008-2185-7 [PubMed: 18548237]
58. Parungo CP, Colson YL, Kim SW, Kim S, Cohn LH, Bawendi MG, Frangioni JV. Sentinel lymph node mapping of the pleural space. Chest. 2005; 127:1799–1804.10.1378/chest.127.5.1799 [PubMed: 15888861]
59. Parungo CP, Ohnishi S, Kim SW, Kim S, Laurence RG, Soltesz EG, Chen FY, Colson YL, Cohn LH, Bawendi MG, Frangioni JV. Intraoperative identification of esophageal sentinel lymph nodes with near-infrared fluorescence imaging. J Thorac Cardiovasc Surg. 2005; 129:844–850.10.1016/j.jtcvs.2004.08.001 [PubMed: 15821653]
60. Hardman R. A toxicologic review of quantum dots: toxicity depends on physicochemical and environmental factors. Environ Health Perspect. 2006; 114:165–172. [PubMed: 16451849]
61. Vakoc BJ, Lanning RM, Tyrrell JA, Padera TP, Bartlett LA, Stylianopoulos T, Munn LL, Tearney GJ, Fukumura D, Jain RK, Bouma BE. Three-dimensional microscopy of the tumor microenvironment in vivo using optical frequency domain imaging. Nat Med. 2009; 15:1219–1223.10.1038/nm.1971 [PubMed: 19749772]
62. McElroy M, Hayashi K, Garmy-Susini B, Kaushal S, Varner JA, Moossa AR, Hoffman RM, Bouvet M. Fluorescent LYVE-1 antibody to image dynamically lymphatic trafficking of cancer cells in vivo. J Surg Res. 2009; 151:68–73.10.1016/j.jss.2007.12.769 [PubMed: 18599080]
63. Gleysteen JP, Newman JR, Chhieng D, Frost A, Zinn KR, Rosenthal EL. Fluorescent labeled anti-EGFR antibody for identification of regional and distant metastasis in a preclinical xenograft model. Head Neck. 2008; 30:782–789.10.1002/hed.20782 [PubMed: 18228526]
64. Mumprecht V, Honer M, Vigl B, Proulx ST, Trachsel E, Kaspar M, Banziger-Tobler NE, Schibli R, Neri D, Detmar M. In vivo imaging of inflammation- and tumor-induced lymph node lymphangiogenesis by immuno-positron emission tomography. Cancer Res. 2010; 70:8842–8851.10.1158/0008-5472.CAN-10-0896 [PubMed: 20978206]
65. Zou P, Xu S, Povoski SP, Wang A, Johnson MA, Martin EW Jr, Subramaniam V, Xu R, Sun D. Near-infrared fluorescence labeled anti-TAG-72 monoclonal antibodies for tumor imaging in colorectal cancer xenograft mice. Mol Pharm. 2009; 6:428–440.10.1021/mp9000052 [PubMed: 19718796]
66. Huyn ST, Burton JB, Sato M, Carey M, Gambhir SS, Wu L. A potent, imaging adenoviral vector driven by the cancer-selective mucin-1 promoter that targets breast cancer metastasis. Clin Cancer Res. 2009; 15:3126–3134.10.1158/1078-0432.CCR-08-2666 [PubMed: 19366829]
67. Grillot-Courvalin C, Goussard S, Huetz F, Ojcius DM, Courvalin P. Functional gene transfer from intracellular bacteria to mammalian cells. Nat Biotechnol. 1998; 16:862–866.10.1038/nbt0998-862 [PubMed: 9743121]
68. Adusumilli PS, Stiles BM, Chan MK, Mullerad M, Eisenberg DP, Ben-Porat L, Huq R, Rusch VW, Fong Y. Imaging and therapy of malignant pleural mesothelioma using replication-competent herpes simplex viruses. J Gene Med. 2006; 8:603–615.10.1002/jgm.877 [PubMed: 16475242]
69. Stiles BM, Adusumilli PS, Bhargava A, Stanziale SF, Kim TH, Chan MK, Huq R, Wong R, Rusch VW, Fong Y. Minimally invasive localization of oncolytic herpes simplex viral therapy of metastatic pleural cancer. Cancer Gene Ther. 2006; 13:53–64.10.1038/sj.cgt.7700860 [PubMed: 16037824]
70. Burton JB, Johnson M, Sato M, Koh SB, Mulholland DJ, Stout D, Chatziioannou AF, Phelps ME, Wu H, Wu L. Adenovirus-mediated gene expression imaging to directly detect sentinel lymph node metastasis of prostate cancer. Nat Med. 2008; 14:882–888.10.1038/nm.1727 [PubMed: 18622403]
71. Serganova I, Ponomarev V, Blasberg R. Human reporter genes: potential use in clinical studies. Nucl Med Biol. 2007; 34:791–807.10.1016/j.nucmedbio.2007.05.009 [PubMed: 17921031]
72. Kishimoto H, Kojima T, Watanabe Y, Kagawa S, Fujiwara T, Uno F, Teraishi F, Kyo S, Mizuguchi H, Hashimoto Y, Urata Y, Tanaka N. In vivo imaging of lymph node metastasis with

telomerase-specific replication-selective adenovirus. Nat Med. 2006; 12:1213–1219.10.1038/nm1404 [PubMed: 17013385]

73. Ntziachristos V, Ripoll J, Wang LV, Weissleder R. Looking and listening to light: the evolution of whole-body photonic imaging. Nat Biotechnol. 2005; 23:313–320.10.1038/nbt1074 [PubMed: 15765087]
74. Swirski FK, Berger CR, Figueiredo JL, Mempel TR, von Andrian UH, Pittet MJ, Weissleder R. A near-infrared cell tracker reagent for multiscopic in vivo imaging and quantification of leukocyte immune responses. PLoS ONE. 2007; 2:e1075.10.1371/journal.pone.0001075 [PubMed: 17957257]
75. Lee KC, Moon WK, Chung JW, Choi SH, Cho N, Cha JH, Lee EH, Kim SM, Kim HS, Han MH, Chang KH. Assessment of lymph node metastases by contrast-enhanced MR imaging in a head and neck cancer model. Korean J Radiol. 2007; 8:9–14. [PubMed: 17277558]
76. Choi SH, Han MH, Moon WK, Son KR, Won JK, Kim JH, Kwon BJ, Na DG, Weinmann HJ, Chang KH. Cervical lymph node metastases: MR imaging of gadofluorine M and monocrystalline iron oxide nanoparticle-47 in a rabbit model of head and neck cancer. Radiology. 2006; 241:753–762.10.1148/radiol.2413051979 [PubMed: 17032913]
77. Paroo Z, Bollinger RA, Braasch DA, Richer E, Corey DR, Antich PP, Mason RP. Validating bioluminescence imaging as a high-throughput, quantitative modality for assessing tumor burden. Mol Imaging. 2004; 3:117–124.10.1162/1535350041464865 [PubMed: 15296676]
78. Zabala M, Alzuguren P, Benavides C, Crettaz J, Gonzalez-Aseguinolaza G, Ortiz de Solorzano C, Gonzalez-Aparicio M, Kramer MG, Prieto J, Hernandez-Alcoceba R. Evaluation of bioluminescent imaging for noninvasive monitoring of colorectal cancer progression in the liver and its response to immunogene therapy. Mol Cancer. 2009; 8:2.10.1186/1476-4598-8-2 [PubMed: 19128467]
79. Servais EL, Colovos C, Kachala SS, Adusumilli PS. Pre-clinical mouse models of primary and metastatic pleural cancers of the lung and breast. Current protocols in pharmacology and drug delivery. 2011 (in press).
80. Zhong XS, Matsushita M, Plotkin J, Riviere I, Sadelain M. Chimeric antigen receptors combining 4-1BB and CD28 signaling domains augment PI3kinase/AKT/Bcl-XL activation and CD8+ T cell-mediated tumor eradication. Mol Ther. 2010; 18:413–420.10.1038/mt.2009.210 [PubMed: 19773745]
81. Luker GD, Luker KE. Optical imaging: current applications and future directions. J Nucl Med. 2008; 49:1–4.10.2967/jnumed.107.045799 [PubMed: 18077528]
82. Miloud T, Henrich C, Hammerling GJ. Quantitative comparison of click beetle and firefly luciferases for in vivo bioluminescence imaging. J Biomed Opt. 2007; 12:054018.10.1117/1.2800386 [PubMed: 17994906]
83. Blasberg RG. In vivo molecular-genetic imaging: multimodality nuclear and optical combinations. Nucl Med Biol. 2003; 30:879–888. [PubMed: 14698792]
84. Dobrenkov K, Olszewska M, Likar Y, Shenker L, Gunset G, Cai S, Pillarsetty N, Hricak H, Sadelain M, Ponomarev V. Monitoring the efficacy of adoptively transferred prostate cancer-targeted human T lymphocytes with PET and bioluminescence imaging. J Nucl Med. 2008; 49:1162–1170.10.2967/jnumed.107.047324 [PubMed: 18552144]
85. Santos EB, Yeh R, Lee J, Nikhamin Y, Punzalan B, La Perle K, Larson SM, Sadelain M, Brentjens RJ. Sensitive in vivo imaging of T cells using a membrane-bound *Gaussia princeps* luciferase. Nat Med. 2009; 15:338–344.10.1038/nm.1930 [PubMed: 19219023]
86. Contag CH, Jenkins D, Contag PR, Negrin RS. Use of reporter genes for optical measurements of neoplastic disease in vivo. Neoplasia. 2000; 2:41–52. [PubMed: 10933067]
87. Jenkins D, Oei Y, Hornig Y, Yu S-F, Dusich J, Purchio T, Contag P. Bioluminescent imaging (BLI) to improve and refine traditional murine models of tumor growth and metastasis. Clin Exp Metastasis. 2003; 20:733–744. [PubMed: 14713107]
88. Haley P, Perry R, Ennulat D, Frame S, Johnson C, Lapointe JM, Nyska A, Snyder P, Walker D, Walter G. STP position paper: best practice guideline for the routine pathology evaluation of the immune system. Toxicol Pathol. 2005; 33:404–407. discussion 408. 10.1080/01926230590934304 [PubMed: 15805080]

89. Van den Broeck W, Derore A, Simoens P. Anatomy and nomenclature of murine lymph nodes: descriptive study and nomenclatory standardization in BALB/cAnNCrl mice. J Immunol Methods. 2006; 312:12–19.10.1016/j.jim.2006.01.022 [PubMed: 16624319]

90. Willard-Mack CL. Normal structure, function, and histology of lymph nodes. Toxicol Pathol. 2006; 34:409–424.10.1080/01926230600867727 [PubMed: 17067937]

91. Yamasaki T, Wakabayashi S, Inoue O, Ando K, Kusakabe K, Kawasaki Y, Okamoto S, Taniguchi M. Specific bio-detection of B16 mouse melanoma in vivo by syngeneic monoclonal antibody. J Invest Dermatol. 1987; 89:225–229. [PubMed: 3624896]

92. Foster PJ, Dunn EA, Karl KE, Snir JA, Nycz CM, Harvey AJ, Pettis RJ. Cellular magnetic resonance imaging: in vivo imaging of melanoma cells in lymph nodes of mice. Neoplasia. 2008; 10:207–216. [PubMed: 18320065]

93. Shu CJ, Radu CG, Shelly SM, Vo DD, Prins R, Ribas A, Phelps ME, Witte ON. Quantitative PET reporter gene imaging of CD8+ T cells specific for a melanoma-expressed self-antigen. Int Immunol. 2009; 21:155–165.10.1093/intimm/dxn133 [PubMed: 19106231]

94. Jansen SA, Conzen SD, Fan X, Krausz T, Zamora M, Foxley S, River J, Newstead GM, Karczmar GS. Detection of in situ mammary cancer in a transgenic mouse model: in vitro and in vivo MRI studies demonstrate histopathologic correlation. Phys Med Biol. 2008; 53:5481–5493.10.1088/0031-9155/53/19/014 [PubMed: 18780960]

95. Wahl RL, Wissing J, del Rosario R, Zasadny KR. Inhibition of autoradiolysis of radiolabeled monoclonal antibodies by cryopreservation. J Nucl Med. 1990; 31:84–89. [PubMed: 2295945]

96. Wang L, Yao Q, Wang J, Wei G, Li G, Li D, Ling R, Chen J. MRI and hybrid PET/CT for monitoring tumour metastasis in a metastatic breast cancer model in rabbit. Nucl Med Commun. 2008; 29:137–143.10.1097/MNM.0b013e3282f258c1 [PubMed: 18094635]

97. Wang Y, Wang W, Li J, Tang J. Gray-scale contrast-enhanced ultrasonography of sentinel lymph nodes in a meta-static breast cancer model. Acad Radiol. 2009; 16:957–962.10.1016/j.acra.2009.03.007 [PubMed: 19427801]

98. Harrell JC, Dye WW, Harvell DM, Pinto M, Jedlicka P, Sartorius CA, Horwitz KB. Estrogen insensitivity in a model of estrogen receptor positive breast cancer lymph node metastasis. Cancer Res. 2007; 67:10582–10591.10.1158/0008-5472.CAN-07-1655 [PubMed: 17975003]

99. Winnard PT Jr, Kluth JB, Raman V. Noninvasive optical tracking of red fluorescent protein-expressing cancer cells in a model of metastatic breast cancer. Neoplasia. 2006; 8:796–806.10.1593/neo.06304 [PubMed: 17032496]

100. Jenkins DE, Hornig YS, Oei Y, Dusich J, Purchio T. Bioluminescent human breast cancer cell lines that permit rapid and sensitive in vivo detection of mammary tumors and multiple metastases in immune deficient mice. Breast Cancer Res. 2005; 7:R444–R454.10.1186/bcr1026 [PubMed: 15987449]

101. Kurihara Y, Watanabe Y, Onimatsu H, Kojima T, Shirota T, Hatori M, Liu D, Kyo S, Mizuguchi H, Urata Y, Shintani S, Fujiwara T. Telomerase-specific virotheranostics for human head and neck cancer. Clin Cancer Res. 2009; 15:2335–2343.10.1158/1078-0432.CCR-08-2690 [PubMed: 19318473]

102. Moral M, Segrelles C, Lara MF, Martinez-Cruz AB, Lorz C, Santos M, Garcia-Escudero R, Lu J, Kiguchi K, Buitrago A, Costa C, Saiz C, Rodriguez-Peralto JL, Martinez-Tello FJ, Rodriguez-Pinilla M, Sanchez-Cespedes M, Garin M, Grande T, Bravo A, DiGiovanni J, Paramio JM. Akt activation synergizes with Trp53 loss in oral epithelium to produce a novel mouse model for head and neck squamous cell carcinoma. Cancer Res. 2009; 69:1099–1108.10.1158/0008-5472.CAN-08-3240 [PubMed: 19176372]

103. Shomura Y, Saito Y, Minami K, Imamura H. A new method for establishing an intrapulmonary tumor in the rabbit. Jpn J Thorac Cardiovasc Surg. 2003; 51:337–343.10.1007/BF02719464 [PubMed: 12962409]

104. Murayama Y, Harada Y, Imaizumi K, Dai P, Nakano K, Okamoto K, Otsuji E, Takamatsu T. Precise detection of lymph node metastases in mouse rectal cancer by using 5-aminolevulinic acid. Int J Cancer. 2009; 125:2256–2263.10.1002/ijc.24707 [PubMed: 19569177]

105. Shah SA, Gallagher BM, Sands H. Lymphoscintigraphy of human colorectal carcinoma metastases in athymic mice by use of radioiodinated B72.3 monoclonal antibody. J Natl Cancer Inst. 1987; 78:1069–1077. [PubMed: 3473248]

106. Ohsawa I, Murakami T, Uemoto S, Kobayashi E. In vivo luminescent imaging of cyclosporin A-mediated cancer progression in rats. Transplantation. 2006; 81:1558–1567.10.1097/01. tp. 0000209448.50238.de [PubMed: 16770245]

107. Stelter L, Amthauer H, Rexin A, Pinkernelle J, Schulz P, Michel R, Denecke T, Stiepani H, Hamm B, Wiedenmann B, Scholz A. An orthotopic model of pancreatic somatostatin receptor (SSTR)-positive tumors allows bimodal imaging studies using 3T MRI and animal PET-based molecular imaging of SSTR expression. Neuroendocrinology. 2008; 87:233–242.10.1159/000111502 [PubMed: 18025811]

108. Hayashi K, Zhao M, Yamauchi K, Yamamoto N, Tsuchiya H, Tomita K, Hoffman RM. Cancer metastasis directly eradicated by targeted therapy with a modified *Salmonella typhimurium*. J Cell Biochem. 2009; 106:992–998.10.1002/jcb.22078 [PubMed: 19199339]

109. Hsieh CL, Xie Z, Yu J, Martin WD, Datta MW, Wu GJ, Chung LW. Non-invasive bioluminescent detection of prostate cancer growth and metastasis in a bigenic transgenic mouse model. Prostate. 2007; 67:685–691.10.1002/pros.20510 [PubMed: 17342752]

110. van Leeuwen AC, Buckle T, Bendle G, Vermeeren L, Valdes Olmos R, van de Poel HG, van Leeuwen FW. Tracer-cocktail injections for combined pre- and intraoperative multimodal imaging of lymph nodes in a spontaneous mouse prostate tumor model. J Biomed Opt. 2011; 16:016004.10.1117/1.3528027 [PubMed: 21280910]

111. Vassallo P, Matei C, Heston WD, McLachlan SJ, Koutcher JA, Castellino RA. Characterization of reactive versus tumor-bearing lymph nodes with interstitial magnetic resonance lymphography in an animal model. Invest Radiol. 1995; 30:706–711. [PubMed: 8748183]

112. La Perle KM, Shen D, Buckwalter TL, Williams B, Haynam A, Hinkle G, Pozderac R, Capen CC, Jhiang SM. In vivo expression and function of the sodium iodide symporter following gene transfer in the MATLyLu rat model of metastatic prostate cancer. Prostate. 2002; 50:170–178.10.1002/pros.10046 [PubMed: 11813209]

113. Nathanson SD, Haas GP, Mead MJ, Lee M. Spontaneous regional lymph node metastases of three variants of the B16 melanoma: relationship to primary tumor size and pulmonary metastases. J Surg Oncol. 1986; 33:41–45. [PubMed: 3762173]

114. Man S, Munoz R, Kerbel RS. On the development of models in mice of advanced visceral metastatic disease for anti-cancer drug testing. Cancer Metastasis Rev. 2007; 26:737–747.10.1007/s10555-007-9087-6 [PubMed: 17846863]

115. Sun R, Zhang JG, Guo CB. Establishment of cervical lymph node metastasis model of squamous cell carcinoma in the oral cavity in mice. Chin Med J Engl. 2008; 121:1891–1895. [PubMed: 19080119]

116. Matsui T, Ota T, Ueda Y, Tanino M, Odashima S. Isolation of a highly metastatic cell line to lymph node in human oral squamous cell carcinoma by orthotopic implantation in nude mice. Oral Oncol. 1998; 34:253–256. [PubMed: 9813718]

117. Maekawa K, Sato H, Furukawa M, Yoshizaki T. Inhibition of cervical lymph node metastasis by marimastat (BB-2516) in an orthotopic oral squamous cell carcinoma implantation model. Clin Exp Metastasis. 2002; 19:513–518. [PubMed: 12405288]

118. Yu Z, Chan MK, Oc P, Eisenberg DP, Shah JP, Singh B, Fong Y, Wong RJ. Enhanced nectin-1 expression and herpes oncolytic sensitivity in highly migratory and invasive carcinoma. Clin Cancer Res. 2005; 11:4889–4897.10.1158/1078-0432.CCR-05-0309 [PubMed: 16000587]

119. Liu J, Blackhall F, Seiden-Long I, Jurisica I, Navab R, Liu N, Radulovich N, Wigle D, Sultan M, Hu J, Tsao MS, Johnston MR. Modeling of lung cancer by an orthotopically growing H460SM variant cell line reveals novel candidate genes for systemic metastasis. Oncogene. 2004; 23:6316–6324.10.1038/sj. onc.12077951207795 [PubMed: 15247903]

120. Doki Y, Murakami K, Yamaura T, Sugiyama S, Misaki T, Saiki I. Mediastinal lymph node metastasis model by orthotopic intrapulmonary implantation of Lewis lung carcinoma cells in mice. Br J Cancer. 1999; 79:1121–1126.10.1038/sj.bjc.6690178 [PubMed: 10098745]

121. Bouvet M, Yang M, Nardin S, Wang X, Jiang P, Baranov E, Moossa AR, Hoffman RM. Chronologically-specific metastatic targeting of human pancreatic tumors in orthotopic models. Clin Exp Metastasis. 2000; 18:213–218. [PubMed: 11315094]

122. Fujihara T, Sawada T, Hirakawa K, Chung YS, Yashiro M, Inoue T, Sowa M. Establishment of lymph node metastatic model for human gastric cancer in nude mice and analysis of factors associated with metastasis. Clin Exp Metastasis. 1998; 16:389–398. [PubMed: 9626818]

123. Mulshine JL, Keenan AM, Carrasquillo JA, Walsh T, Linnoila RI, Holton OD, Harwell J, Larson SM, Bunn PA, Weinstein JN. Immunolymphoscintigraphy of pulmonary and mediastinal lymph nodes in dogs: a new approach to lung cancer imaging. Cancer Res. 1987; 47:3572–3576. [PubMed: 3472655]

124. Ueno H, Hihara J, Shimizu K, Osaki A, Yamashita Y, Yoshida K, Toge T. Experimental study on fluorescent microspheres as a tracer for sentinel node detection. Anticancer Res. 2005; 25:821–825. [PubMed: 15868914]

125. Troyan SL, Kianzad V, Gibbs-Strauss SL, Gioux S, Matsui A, Oketokoun R, Ngo L, Khamene A, Azar F, Frangioni JV. The FLARE intraoperative near-infrared fluorescence imaging system: a first-in-human clinical trial in breast cancer sentinel lymph node mapping. Ann Surg Oncol. 2009; 16:2943–2952.10.1245/s10434-009-0594-2 [PubMed: 19582506]

126. Long CM, van Laarhoven HW, Bulte JW, Levitsky HI. Magnetovaccination as a novel method to assess and quantify dendritic cell tumor antigen capture and delivery to lymph nodes. Cancer Res. 2009; 69:3180–3187.10.1158/0008-5472.CAN-08-3691 [PubMed: 19276358]

127. Koyama Y, Talanov VS, Bernardo M, Hama Y, Regino CA, Brechbiel MW, Choyke PL, Kobayashi H. A dendrimer-based nanosized contrast agent dual-labeled for magnetic resonance and optical fluorescence imaging to localize the sentinel lymph node in mice. J Magn Reson Imaging. 2007; 25:866–871.10.1002/jmri.20852 [PubMed: 17345640]

128. Wahl RL, Kaminski MS, Ethier SP, Hutchins GD. The potential of 2-deoxy-2[18F]fluoro-D-glucose (FDG) for the detection of tumor involvement in lymph nodes. J Nucl Med. 1990; 31:1831–1835. [PubMed: 2230996]

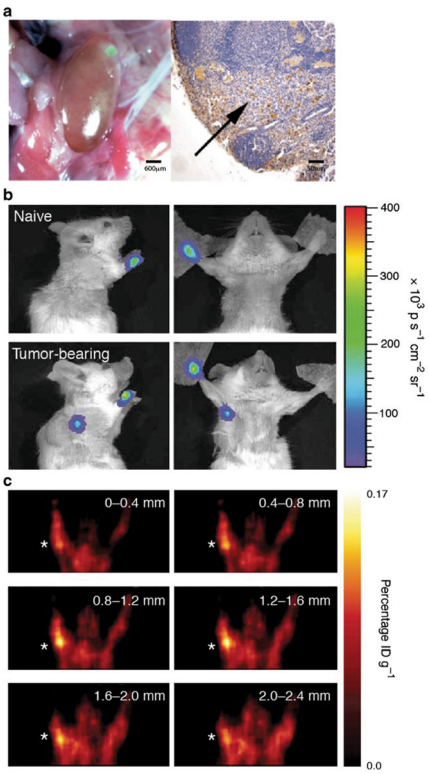

Fig. 1.

Oncolytic virus-mediated detection of lymph node metastases using either fluorescent imaging, BLI, or PET. **a** Fluorescence microscopy detects LNM in cervical LN following injection of GFP-expressing herpes virus (*left panel*). Histology confirms microscopic focus of LNM as denoted by an *arrow* (*right panel*) (reprinted with permission from Adusumilli et al. [30], © 2006 American Association for Thoracic Surgery). **b** BLI signal is seen in the axillary region of mice following injection of a firefly luciferase containing recombinant adenovirus in mice containing prostate cancer LNM (reprinted with permission from Macmillan Publishers Ltd., Burton et al. [70]). **c** Similarly, a prostate-specific PET reporter vector facilitated PET identification of LNM following primary tumor resection in conjunction with the injection of ^{18}FHBG tracer (reprinted with permission from Macmillan Publishers Ltd., Burton et al. [70])

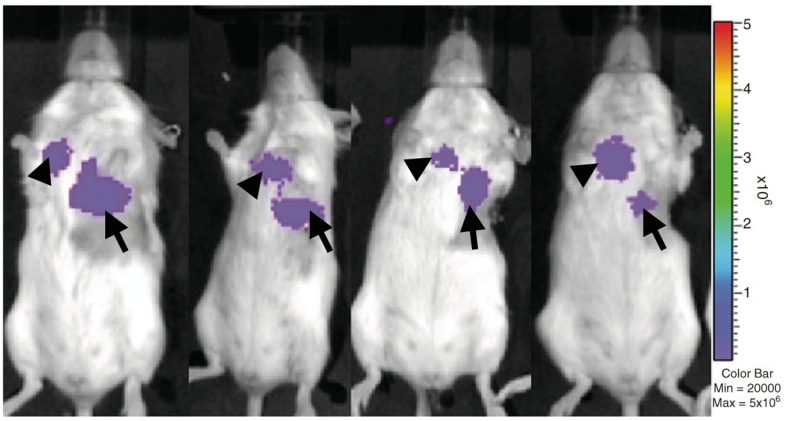

Fig. 2.

BLI detects mediastinal lymph node metastases in an orthotopic mouse model of primary lung cancer. eGFP-firefly luciferase-expressing lung cancer cells were directly injected into lung parenchyma to create an orthotopic lung cancer primary tumor (*arrows*). Within 2–3 weeks, mediastinal BLI signal reveals lymph node metastases in the typical lymphatic drainage pathway (*arrowheads*).

Mediastinal LNM was confirmed in each mouse upon necropsy using H&E and IHC for tumor markers

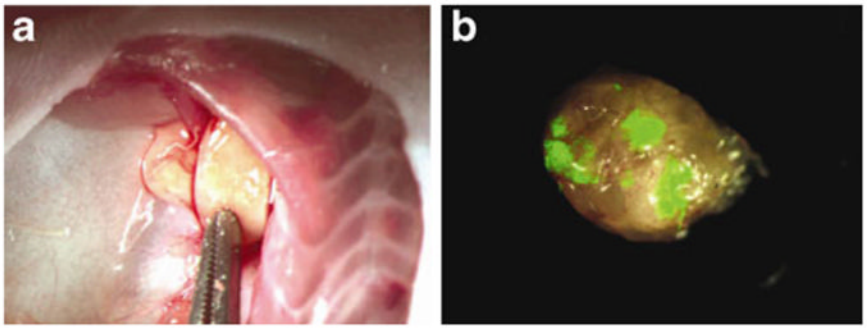

Fig. 3.

Fluorescently guided identification of metastatic foci within enlarged lymph nodes. **a** Orthotopic implantation of breast cancer results in enlarged axillary LN. **b** Ex vivo analysis of an enlarged axillary LN with fluorescent imaging reveals metastatic foci [26] (Eisenberg et al., “Real-time intraoperative detection of breast cancer axillary lymph node metastases using a green fluorescent protein-expressing herpes virus”, *Ann Surg*, 243(6), 824–30)

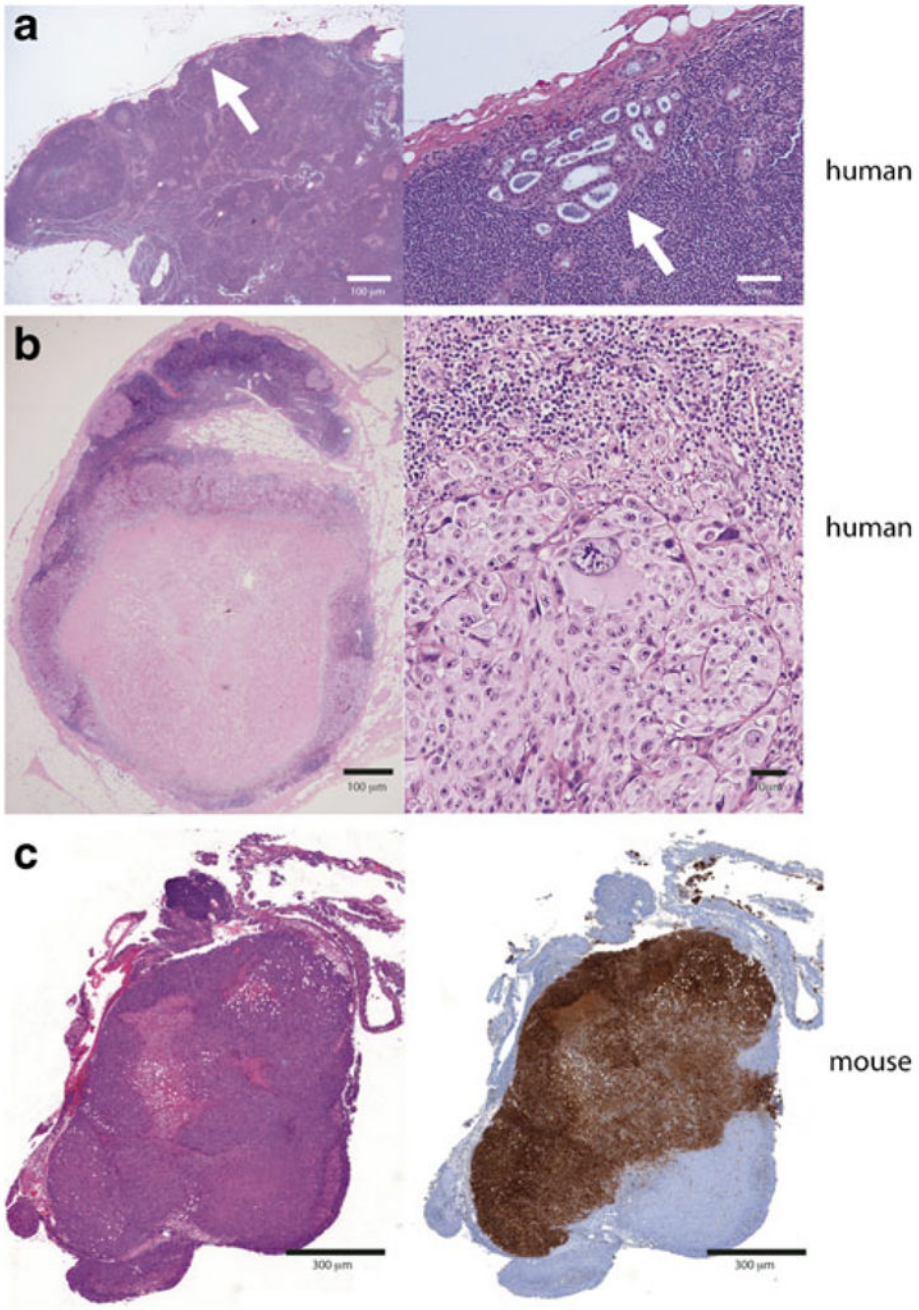

Fig. 4.

Metastatic human and murine lymph nodes exhibiting a spectrum of involvement. **a** Human metastatic breast cancer with focal lymph node involvement (*arrow*) at low (*left*) and high power (*right*) showing preservation of lymph node architecture. **b** Metastatic melanoma replacing a regional lymph node and obscuring architectural features at low (*left*) and high (*right*) powers. **c** Murine lymph node replaced by tumor, H&E (*left*), immunohistochemistry (*right*)

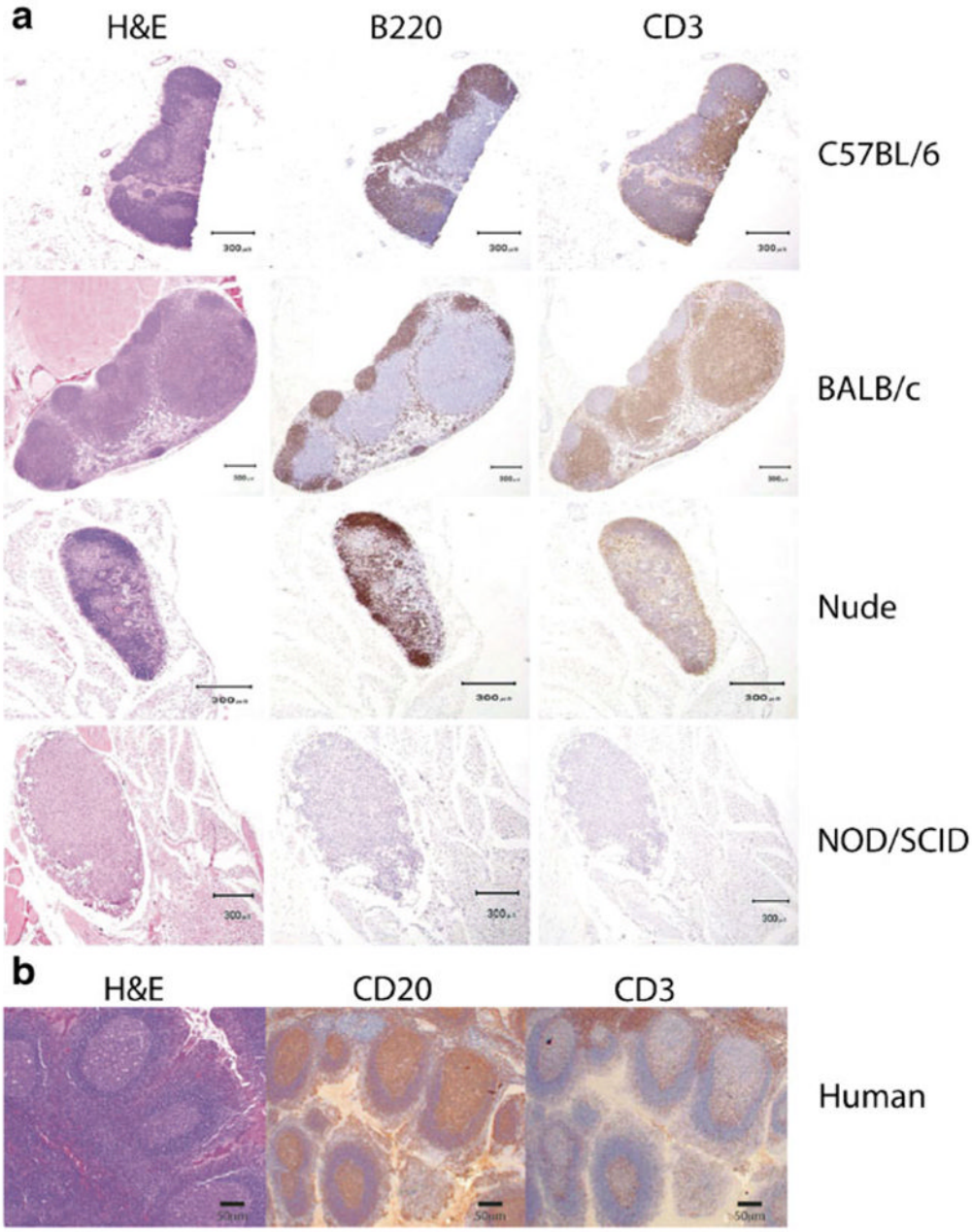

Fig. 5.

Immunohistochemical characterization of murine and human lymph nodes to assist in the identification of lymph nodes in murine models. **a** H&E and immunohistochemistry for B cells (B220) or T cells (CD3) in immunocompetent mouse strains (C57/B6 and BALB/c) and immunodeficient strains (nude athymic and NOD/SCID gamma). **b** H&E and immunohistochemistry for CD20 (B cells) and CD3 (T cells) in human lymph nodes

Table 1

Animal models of cancer used in lymph node metastasis imaging studies

Primary tumor	Animal model	Cell line[b]	Model type	Route	Time to LN metastases	Identification method	Lymph nodes evaluated	Yield/sensitivity/specificity
Melanoma	C57BL/6 mice [91]	B16	IC, S, O	Flank	NR	LS	Axillary	
	C57BL/6 mice [13, 14]	B16-BL6 (5×10^6)	IC, S, O	Auricular	20 days	FL	Cervical	LN yield: 6/7 LN
	C57BL/6 mice [15]	B16-F10 (2×10^6)	IC, S, O	Thigh	14–21 days	LS	NR[a]	Yield, 17/17 mice
	C57BL/6 mice [16]	B16-F10 (2×10^6)	IC, S, O	Hind leg	7–28 days	MRI	Para-aortic/pelvic[a]	LN yield, 100% mice
	C57BL/6 mice [92]	B16-F10 (1×10^5)	IC, S, O	Abdominal SQ	15 days	MRI	Axillary, cervical, inguinal[a]	
	C57BL/6J-TyrC-2J/J mice C57BL/6 mice [9–12, 93]	B16-F10 (2×10^5)	IC, S, O	Footpad	21 days	BLI, MRI, PET	Popliteal, inguinal, brachial axillary[a]	
	MeLiM Swine [20]	Naturally occurring	IC, S, O	Spontaneous	NR	PET	NR	
	Nude athymic mice [19]	M21	ID, X, O	Thigh	NR	FL	Axillary, inguinal	
	Nude athymic mice [18]	B16CXC4	ID, X, O	Lip	NR	NIRF	Cervical	
	Nude athymic mice [17]	B16-F10 (1×10^6)	ID, X, O	Auricular	7 days	US	Cervical[a]	
	Sinclair swine [21, 22]	Naturally occurring	IC, S, O	Spontaneous	NR	LS, US	Axillary, cervical, inguinal	Yield, 6/6 swine (27/31 LN)
Breast	BALB-neuT mice [25]	Transgenic	TG	–	21 weeks	MRI	Axillary[a]	
	C3(1) SV40 tag mice [94]	Transgenic	TG	–	12 weeks	MRI	Axillary[a]	Yield, 12/12 mice
	Lewis rats [95]	Disaggregated rodent tumor	IC, S, O	Mammary fat pad	NR	PET	Popliteal	
	New Zealand white rabbits [96, 97]	VX2 (1×10^7)	IC, S, O	Intramammary pocket	30–50 days	MRI, PET, US, XR	Axillary, mediastinal, abdominal	MRI sensitivity, 78%, PET/CT; sensitivity, 68%, MRI/PET/CT; sensitivity, 82%; US sensitivity, 23.5%; XR sensitivity, 0%
	Nude athymic mice [23, 24, 66, 98–100]	KPL1, MCF-7, MDA-MB231, MDA-MB435, PT-18, T47D (1×10^6–1×10^7)	ID, X, O	Mammary fat pad	15–90 days	BLI, FI, MRI	Brachial, axillary, cervical, lateral thoracic, iliac, abdominal, inguinal[a]	Yield, 100% mice by week 8
	Nude athymic mice [26, 27]	MDA-MB435 (2×10^6)	ID, X, O	Intramammary pocket	70–100+days	FI	Axillary[a]	Yield, 11/20 LN sensitivity/specificity, 80/96%
	Nude athymic mice [100]	MDA-MB231 (1×10^5)	ID, X, H	Intracardiac	35 days	BLI	Brachial, axillary[a]	Yield, 5/8 mice

Primary tumor	Animal model	Cell line[b]	Model type	Route	Time to LN metastases	Identification method	Lymph nodes evaluated	Yield/sensitivity/specificity
Head and neck	BALB/c nu/nu mice [101]	SAS-L, HSC-3 (1×10^5)	ID, X, O	Tongue	24 days	FL	Head/neck[a]	Yield, 13/14 LN; sensitivity/
	C57/B Bk5myrAkt mice [102]	Spontaneous	IC, S, O	–	21 days	PET	NR	specificity, 92%/87%
	Nude athymic mice [29]	DM14 (2×10^5)	ID, X, O	Tongue	15 days	MRI, NIR	Cervical[a]	Yield, 4/6 LN
	NZ white rabbits [75, 76]	VX2 ($1–2\times10^7$)	IC, S, O	Auricular	21–28 days	MRI, NIR	Cervical, mandibular[a]	Sensitivity/specificity,
	SCID mice [63]	OSC-19 (2×10^5), SCC1 (2×10^6)	ID, X, O	Tongue	14 days	FL	Yield, 8/8 mice	72–100%/83–85%
Lung/mesothelioma	Japanese white rabbits [103]	VX1	IC, S, H	Transbronchial	34 days	XR	Pulmonary	Yield, 1/22 rabbits
	Nude athymic mice [30]	MSTO-211 H (1×10^5)	ID, X, H/O	Preauricular, pleural	28–56 days	FL	Cervical, mediastinal, abdominal, retoperitoneal[a]	
	SCID mice [32]	MA44-33 (2×10^6)	ID, X, O	Intraparenchymal	12 days	FL	Mediastinal	Yield, 5/6 mice
	BALB/c nude mice [104]	HT-29 (5×10^6)	ID, X, O	Submucosal anorectal	35 days	FL	Para-aortic[a]	Sensitivity/specificity, 100%
	b-estriol pre-treated athymic mice [105]	LS174T (4×10^6)	ID, X, H	Footpad	24 days	LS	Axillary, popliteal[a]	Yield, 66%
	b-estriol pre-treated athymic mice [105]	LS174T (4×10^6)	ID, X, H	IV	35 days	LS	Axillary, popliteal[a]	Yield, 66%
	C57BL/6 mice [36]	Bx-PC (1×10^6)	IC, S, O	Portal vein	36 days	FL	Portal vein[a]	
Gastrointestinal	F344 rats, Lewis rats [106]	RCN-H4 (5×10^6)	IC, S, O	Ileocolic vein	50 days	BLI	Mesenteric	Yield, 3/10 mice
	F344/N Jcl-rnm nude rats [34, 35]	OCUM-2M (1×10^6)	ID, X, O	Subserosal gastric	NR	FL	Gastric/hepatic[a]	Yield, 100% rats
	NMRI nude mice [107]	AR42J (1×10^6)	ID, X, O	Amphicrine	NR	PET, CT	Mesenteric[a]	
	Nude mice [36, 37]	MIA-PaCa2 (SOI)	ID, X, O	Pancreatic	36 days	BLI, FL	Portal, intestinal[a]	
	Nude mice [108]	XPA1-RFP (5×10^5)	ID, X, H	Inguinal LN	7 days	FL	Axillary[a]	
	SCID/bg mice [87]	HT-29($1–3\times10^6$)	ID, X, H	SQ flank	14–21 days	BLI	Axilliary[a]	Yield, 9/18 mice
	nu/nu mice, NOD/SCID [38, 39]	PC3M, PC3M-SV1, PC3M-LN4 (5×10^5)	ID, X, O	Prostate	7–14 days	BLI, FL	Pelvic	Yield, 20–100%
Prostate	C57LB/6xFBV mice [109, 110]	Transgenic	TG	–	16–24 weeks	BLI, FL, LS	Pelvic	Yield, 40%
	Copenhagen rats [111]	R3327-MATLyLu (1×10^6)	IC, S, H	Flank	14 days	MRI	Popliteal[a]	Yield, 18/21 LN

Primary tumor	Animal model	Cell line[b]	Model type	Route	Time to LN metastases	Identification method	Lymph nodes evaluated	Yield/sensitivity/specificity
	Copenhagen rats [112]	R3327-MATLyLu (1×10^6)	IC, S, H	Footpad	7–23 days	LS	Axillary[a]	Yield, 3/12 LN

IC immunocompetent, *ID* immunodeficient, *S* syngeneic, *X* xenogeneic, *TG* transgenic, *H* heterotopic, *O* orthotopic, *BLI* bioluminescent imaging, *CT* computer tomography, *FL* fluorescence imaging/microscopy, *LS* lymphoscintigraphy, *MRI* magnetic resonance imaging, *NIR* near IR fluorescence, *PET* positron emission tomography, *US* ultrasound, *XR* X-ray

[a] Micrometastatic disease

[b] Cancer cell line (number of cells typically injected)

Table 2

Tumor cell lines predisposed to LNM

Cancer	Cell line	Parent cell line	Origin	Histology	Yield[a]
Melanoma	B16-BL6 [113]	B16	C57BL/6J	Cutaneous	42–72% mice
	B16-F10 [113]	B16	C57BL/6J	Cutaneous	18–82% mice
Breast	MDA-MB-231(LM1) [114]	MDA-MB-231	Human	Adenocarcinoma	92% LN
	MDA-MB-435(LN435) [26]	MDA-MB-435	Human	Adenocarcinoma	NR
Head and neck	GDC185 [115]	–	Human	Squamous carcinoma	56–81% LN
	HSC-3-M3 [116]	HSC-3	Human	Squamous carcinoma	90% mice
	OSC-19 [117]	–	Human	Squamous carcinoma	81% mice
	MG14 [118]	SCC7	C3H/HeJ	Squamous carcinoma	NR
Lung	H460SM [119]	H460	Human	Adenocarcinoma	100% rats
	LLC [120]	–	C57BL/6	Adenocarcinoma	93% mice
	Ma44-3 [32]	Ma44	Human	Squamous carcinoma	83% mice
Gastrointestinal	MIA-PaCa2 [121]	–	Human	Ductal adenocarcinoma	NR
	OCUM-2M-LN [122]	OCUM	Human	Scirrhous carcinoma	100% mice
Prostate	PC3-LN4 [38]	PC-3	Human	Adenocarcinoma	100% mice

LN lymph node, *NR* not recorded

[a] Pathologically confirmed metastases

Table 3

Preclinical lymphatic/SLN imaging

Imaging modality	Animal model	Lymph node tracer	Route	Tracer administration to imaging time	Tracer size[a]	Depth of penetration	Nodal specificity[b]	Clinical translatability and comments
Visual	Dogs, normal lung [40]	Isosulfan Blue + Tc-99 m	Intrapulmonary	5–20 min	100–1000 nm	N/R	5/6 dogs, identified pulmonary, tracheobronchial, and mediastinal LN	Approved for human use; current standard in breast cancer and melanoma; limited use in other tissue such as lung
	Pigs, normal mammary glands [47]	Blue dye liposomes	Mammary gland	3–24 h	100–1,000 nm	N/R	SLN detected in all animals up to 24 h	Approved for human use; improved nodal staining compared to free blue dye
Radioisotope	Rabbits, hind leg popliteal nodes [50]	Tc-99m-labeled liposomes	SQ	0.5–24 h	~130 nm	N/R	N/R	Approved for human use; therapeutic potential
	Dogs, normal lung [123]	I-131-labeled mob	Bronchosopic delivery	14–36 h		N/R	N/R	Human toxicities unknown; able to direct tracers to specific LN basins
Ultrasound	Dogs, normal cervical and popliteal nodes [52]	Nanobubbles	SQ	0–120 min	500–1,000 nm	2 cm	34/40 LN 30/32 LN (near micron/ submicron bubbles)	Nanobubbles not approved for human use; concern for thermal injury to normal tissue
	Mice, footpad [41]	Evans blue dye	Intradermal	8 s–1.5 h		3 cm	N/R	Blue dye and ultrasound approved for human use
	Dogs, normal axillary and inguinal lymph nodes [51]	Gold nanotubes	SQ	19–46 h	10×400 nm	> 1.8 nm	N/R	Sonovue approved for human use

Imaging modality	Animal model	Lymph node tracer	Route	Tracer administration to imaging time	Tracer size[a]	Depth of penetration	Nodal specificity[b]	Clinical translatability and comments
Fluorescent imaging	Rats, footpad and pigs, GI tract [124]	Fluorescent microspheres	SQ footpad, submucosal	0.2–6 h	100–1,000 nm	N/R	5/6 esophageal and small bowel SLN; 1/6 gastric and large bowel SLN	Not approved for human use
	Pigs, normal colonic mesenteric nodes [125]	ICG:HAS	Colonic parenchyma	~5 min	~7 nm[1]	<4 cm	Mesenteric SLN identified in 5/5 pigs	ICG:HAS approved for human use; FLARE system in clinical trial for breast cancer SLN mapping
	Mice, subcutaneous melanoma and teratocarcinoma [19]	QDs	IT	0–40 min	22–40 nm[1]	N/R	N/R	QDs not approved in humans, toxicity unknown
	Rats and pigs, pleural lymphatics [58]	QDs	Intrapleural	4–24 h	15 nm[1]	N/R	N/R	QDs not approved for human use; intraoperative NIR fluorescent imaging system easily adaptable for human use
	Pigs, lung [43]	QDs	Lung parenchyma	1 min–4 h	15–20 nm[1]	1.5–5 cm	16/16 SLN	QDs not approved for human use
OFDI with intravital microscopy	Mice, dorsal skin fold sarcoma [61]	No tracer	N/A	N/A		1–2 mm	N/R	Identified cellular masses within peritumoral lymphatics

FLARE fluorescence-assisted resection and exploration, *ICG* indocyanine green, *HAS* human serum albumin, *IT* intratumoral, *QDs* quantum dots, *LN* lymph node, *SLN* sentinel lymph node, *SQ* subcutaneous, *N/R* not recorded, *OFDI* optical frequency domain imaging, *GI* gastrointestinal

[a] Size of tracer agent as reported

[b] Number of LN correctly identified or number of animals with positive LNs

[1] Hydrodynamic diameter

J Mol Med (Berl). Author manuscript; available in PMC 2012 August 1.

Table 4

Preclinical LNM imaging

Imaging modality	Animal model	Lymph node tracer	Route	Tracer administration to imaging time	Tracer size[a]	Depth of penetration	Nodal specificity[b]	Clinical translatability and comments
Fluorescent imaging	Mice, inguinal and axillary nodes from subcutaneous tumor model [62]	Fluorescent-labeled LYVE-1 mAb; RFP-pancreatic cancer cells	SQ	4–72 h		N/R	N/R	Not approved for human use; monoclonal LYVE-1 antibody targets lymphatics and co-localizes with RFP-expressing metastatic cancer cells
	Mice, oral squamous carcinoma [63]	Cy5.5-labeled anti-EGFR mAb	IV	72 h		N/R	8/8 biopsies	Cy5.5 not approved for human use
	Mice, breast cancer [26]	GFP-expressing oncolytic herpes virus NV1066	IT	48 h		N/R	4/5 LN	GFP not approved for human use; therapeutic potential
	Mice, orthotopic pleural mesothelioma [30]	GFP-expressing oncolytic herpes virus NV1066	Intrapleural	48 h		N/R	80% sensitivity	Lymph node metastases identified by GFP–fluorescent thoracoscope; therapeutic potential
	Mice, orthotopic rectal cancer [72]	GFP-expressing telomerase-specific oncolytic adenovirus	IT	5 days		N/R	12/13 LN	GFP not approved for human use; therapeutic potential
	Mice, hindpaw colon cancer model [74]	VT680-labeled lymphocytes	IV	7–9 days		5 mm	N/R	Not approved for human use
MRI	Mice, B16 melanoma footpad [126]	SPIO-labeled tumor cells	SQ	0–9 days		N/A	N/R	SPIO approved for use in humans
	Mice, breast cancer [25]	Gd-labeled dendrimers	IT	12–36 min	9–13 nm	N/A	6/6 mice; identified metastatic LN	MRI and gadolinium approved for human use;

J Mol Med (Berl). Author manuscript; available in PMC 2012 August 1.

Imaging modality	Animal model	Lymph node tracer	Route	Tracer administration to imaging time	Tracer size[a]	Depth of penetration	Nodal specificity[b]	Clinical translatability and comments
								dendrimers not approved for human use
	Mice, normal mammary glands [127]	Gd/Cy5.5 dual-labeled dendrimers	Mammary gland	20–30 min	9 nm	N/A	N/R	Dendrimers not approved for human use; dual-imaging technique with NIR fluorescence
PET	Rats, subcutaneous ovarian and lymphoma xenografts [128]	FDG PET	IV	20 min–2 h		N/A	N/R	FDG PET approved for human use
	Mice, footpad melanoma [9]	FEAU; oncolytic herpes virus NV1023	IT	2 h		N/A	8/8 LN	PET approved for human use; limited by high background PET signal in primary tumor and GI tract
BLI	Mice, mammary gland [66]	D-Luciferin; firefly luciferase-expressing adenoviral vector	IT	20 min		N/A	N/R	D-Luciferin not approved for human use
	Mice, pleural tumors [79]	D-Luciferin; firefly luciferase-expressing tumors	IP	20 min		N/A	N/R	D-Luciferin not approved for human use

BLI bioluminescent imaging, *FDG* 2-deoxy-2[^{18} F]Fluoro-D-Glucose, *FLARE* fluorescence-assisted resection and exploration, *GFP* green fluorescent protein, *IP* intraperitoneal, *IT* intratumoral, *IV* intravenous, *mAb* monoclonal antibody, *MRI* magnetic resonance imaging, *NIR* near infrared, *PET* positron emission tomography, *SCID* severe combined immunodeficiency, *SLN* sentinel lymph node, *SQ* subcutaneous, *N/R* not recorded, *OFDI* optical frequency domain imaging, *SPIO* small paramagnetic iron oxide

[a] Size of tracer agent as reported

[b] Number of LN correctly identified or number of animals with positive LNs